Design and Characterisation of Cross-sectional Geometries for Soft Robotic Manipulators with Fibre-reinforced Chambers

Jialei Shi[1], Wenlong Gaozhang[1] and Helge A. Wurdemann[1]

Abstract— Fluid elastomer actuators are a prevalent design paradigm in the field of soft robotics. To prevent the elastomer from ballooning and increase the actuation consistency, a fibre-reinforced design is commonly utilised, with the effect of the fibre angle on the robot's performance well established. However, the impact of the geometry of the fibre-reinforced chambers has not been tested. This paper explores two chamber geometries, circular and semi-circular, using measurements in alignment with minimally invasive surgery (MIS) to determine if there is a difference in performance. The fabrication process of robots with different chamber geometries is first streamlined, then the characterisation of each robot is experimentally identified. The results show the chamber geometry plays an important role in affecting the performance of the robots, e.g., with a stiffness variation greater than 20% between the two designs.

I. INTRODUCTION

Soft robots are partially or wholly built using soft compliant materials. The inherent compliance of these materials enables the robots to mitigate uncertainty [1], achieve safe interaction with the environment [2] and have dexterous manoeuvrability [3], [4]. To construct soft robots, elastomers with a high elongation ratio ($> 700\%$) and various shore hardness ranges (00-10 $\sim$ 40A) [5], [6] are typically used. To actuate such elastomer-based robots, fluidic elastomer actuators (FEAs) driven by fluids are prevalent [7].

A general fabrication methodology for the design and fabrication of the FEAs is summarised in [8], which elaborates different design morphologies to implement compliant locomotion and movement. In [9], different geometry ratios and channel designs of FEAs are investigated to optimize the bending angle, maximum stress generated, and radial expansion (or ballooning). This ballooning effect may have a functional effect, e.g., requiring lower actuation pressure (< 0.6 bar) or anchoring the robot [10]. Ballooning may also introduce actuation inconsistency, interfere with embedded sensors and can put the robot at risk of bursting. To prevent the elastomer from ballooning, fibre-reinforced design of each actuation chamber was first proposed in [11], and has since been established in different applications, such as marine grasping manipulators [12], minimally invasive surgery (MIS) [13], [14] and interventional tools [15], assistive technologies [16]–[18] and rotary actuators [19].

[1]Jialei Shi, Wenlong Gaozhang and Helge A. Wurdemann are with the Department of Mechanical Engineering, University College London, UK. h.wurdemann@ucl.ac.uk
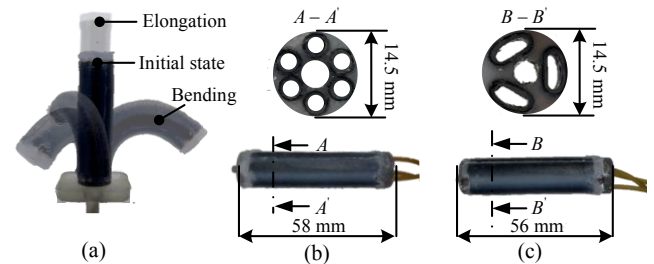
Fig. 1. Overview of two robots with different chamber geometries. (a) The manipulators response under different actuation includes elongation and omni-directional bending. (b) Type-1 robot with three identical circular chamber pairs. (c) Type-2 robot with three identical semi-circular chambers.

The concept is to wrap in-extensible fibre around the FEAs to restrain the radial expansion while allowing longitudinal elongation. This design mitigates the ballooning, allows miniaturised soft robotic manipulators, in MIS for instance, and then produces robots with a higher force capability based on higher actuation pressure up to 2.5 bar, when compared to unreinforced chambers [8].

Previous research has investigated the characterisations of fibre-reinforced FEAs. The influence of the fibre angle is addressed by [20], which proposed a flexible, serially-connected robot with locomotion ability by mechanically programming the fibre angle. The stiffness identification and modelling of the FEAs was done in [21], which observed that the stiffness of the FEAs was proportional to the pressurisation. Instead of constraining the radial expansion of the robot body, researchers investigated how the pressurisation influences the unreinforced chambers [22]. A fibre-reinforced chamber design was proposed, which improves the performance of actuation consistency, compared with the robot having unreinforced chambers in [23]. The design considerations of FEAs with fibre-reinforced chambers are further reviewed in [24], [25]. In summary, chambers with a fibre-reinforced design are shown to have the highest actuation consistency. Although the research in [9], [26]–[28] has demonstrated that the cross-sectional geometry of the actuation chambers is important, e.g., for miniaturising the dimension of FEAs and optimising the bending angle, the impact of the geometry of individually fibre-reinforced actuation chambers has not been investigated.

This paper explores different cross-sectional geometrical designs for individually fibre-reinforced actuation chambers in miniaturised fluidic-driven soft robotic manipulators. Our area of application is minimally invasive procedures. Here, medical instruments are inserted through $12 - 15\,\text{mm}$ inci-

sions, known as Trocar ports allowing surgeons to carry out essential surgical interventions inside the patient's body [29]. In particular, we explore two chamber geometries: a circular (defined as a type-1 robot) and a semi-circular chamber (defined as a type-2 robot). The details of the robots' designs are shown in Fig. 1. The design and fabrication process of soft robots with different chamber geometries is first generalised. The characterisation of each robot is then identified and compared through testing to determine the influence of chamber geometry and provide insight into how chamber geometry can vary the performance of soft robots.

This paper is organised as follows: Section II describes the design considerations of the robots and discusses how the fabrication process can be streamlined. Section III presents and analyses the experimental results of the main characterisations of the type-1 and type-2 robot. The conclusions and potential for future research are summarised in Section IV.

II. DESIGN, FABRICATION AND, ASSESSMENT CRITERIA

The actuation paradigm adopted here includes three sets of chambers evenly distributed around the centre axis to achieve both elongation and omni-directional bending in line with [24]. This continuum type of soft robot has an elongation capability that further enlarges the reachable workspace and enhances the tip dexterity. However, there are a few specific surgical and practical requirements to be considered.

A. Principles of Design

1) Dimension Requirements: Considering requirements emerging from a potential application in single port abdominal surgery, the diameter of a soft robot should be smaller than 15 mm (the largest commercially available Trocar), with a lumen in the range of $4 \sim 5$ mm to accommodate the mounting of surgical tools [30]. The measurements used for the robots discussed in this paper are a 14.5 mm outer diameter D_r with a 4.5 mm inner lumen D_l (see Fig. 2).

2) Actuation and Fabrication: The silicone used in the construction of the robot should have a sufficient thickness to guarantee a successful fabrication. For example, it is necessary to ensure the demoulding process will not unexpectedly tear the robot, especially when the chamber moulds are removed. The minimum thickness of silicone to the edge is defined as δ in this paper and shown in Fig. 2. A smaller chamber diameter can facilitate the fabrication but will require greater actuation pressure; this will compromise the actuation efficiency. Given the body dimensions have been determined in Section II-A.1, the chamber diameter is maximised while ensuring that the margin of the silicone thickness is sufficient. As such, δ_1 of the type-1 robot is empirically chosen as 0.65 mm, and the resulting maximum chamber diameter is 2.50 mm. To make the two types of robot comparable, the equivalent chamber area A_2 of the type-2 robot is designed approximately equal to one chamber pair of the type-1 robot. This yields $A_2 \approx 2A_1$, and the 2% discrepancy is considered negligible. The detailed dimensions of each robot can be found in Fig. 2.

B. Process of Fabrication

The generalised fabrication of the two types of robots are the same, consisting of the three steps summarised in Fig. 3. The reusable moulds are 3D-printed using resin Tough-2000 (Formlabs Form 3) because the printing accuracy can be guaranteed, and this resin is suitable for prototyping sturdy parts without compromising the resilience. The only difference between fabricating each type of robot is that the chamber moulds (highlighted in blue in Fig. 3) vary in shape, and the two adjacent chambers of the type-1 robot are connected by 1 mm diameter silicone pipe in the procedure (b). The interchangeability of moulds reduces the cost and fabrication time, e.g., the outermost moulds can be shared by each type of robot (yellow cylindrical walls in Fig. 3(a)). To maximise elongation capability and guarantee consistency of the fibre winding, the fibre is weaved densely with its direction perpendicular to the central axis [20]. The fabricated manipulators can also be serially connected to achieve greater dexterity.

C. Assessment Criteria

1) Response-to-actuation Ratio: To assess the actuation efficiency, the response-to-actuation ratio β is defined as the value of response denoted by Ω, which can be elongation, bending angle and generated force, divided by the generalised actuation pressure P. This yields in (1).

$$\beta = \frac{\Omega}{P}, \text{ and } P = \frac{p_1 + p_2 + p_3}{3} \qquad (1)$$

The vector of chamber pressure is $p = (p_1, p_2, p_3)$. In this way, the elongation ratio-to-actuation ratio is defined as β_e, the bending angle-to-actuation ratio is defined as β_b and the force-to-actuation ratio is defined as β_f.

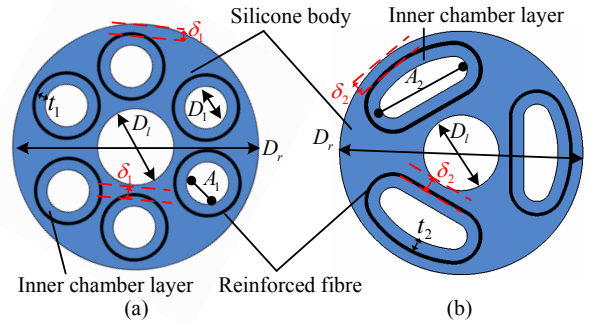|				
	t_1	Thickness of inner chamber layer	0.60 mm
	δ_1	Minimum thickness of silicone	0.65 mm
Type-1	D_1	Diameter of the chambers	2.50 mm
	A_1	Area of one circular chamber	4.91 mm^2
	t_2	Thickness of inner chamber layer	0.70 mm
Type-2	δ_2	Minimum thickness of silicone	0.75 mm
	A_2	Area of one semi-circular chamber	10.01 mm^2

Fig. 2. Dimension and structure of the cross-section of each soft robot. (a) Type-1: the robot has six identical circular chambers with two adjacent connected chambers, allowing three chamber pairs actuate individually. (b) Type-2: the robot has three identical semi-circular chambers, with each chamber actuated individually.

2) Hysteresis Ratio: Hysteresis has been observed in elastomer-based materials, which indicates the response is dependent on the direction of the change of actuation [23], [25]. Considering this, the hysteresis ratio here is calculated by taking the area between the forward and backward actuation curves, and normalizing it by dividing it by the maximum response. This yields in (2).

$$h = \frac{|\Omega_f - \Omega_b|}{\Omega_m} \times 100\% \qquad (2)$$

Ω_f is the response of the forward, Ω_b the response of the backward actuation process. Ω_m is the maximum response. The hysteresis ratio of elongation and bending can then be defined as h_e and h_b, respectively. In this way, β_e, β_b, h_e, h_b are utilised to assess and compare the performance of each robot design in Section III.

III. EXPERIMENTAL CHARACTERISATION AND COMPARISON

A. Experimental Setup

Each robot design under investigation shares the same setup. The pressure in each chamber is regulated by a pressure regulator (Camozzi K8P), the output pressure of
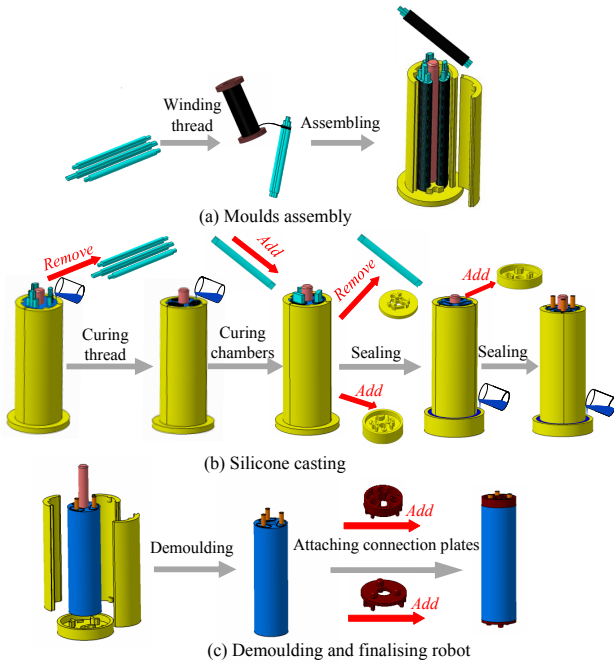

Fig. 3. Fabrication of each robot design: $(a) \rightarrow (b) \rightarrow (c)$. Please note the chambers shown here are from the type-2 robot. (a) Moulds assembly: One set of chamber moulds is comprised of an inner core and two identical slide parts. In-extensible thread is manually wound around the assembled chamber moulds before assembling all moulds. (b) Silicone curing: after pouring the silicone (EcoFlex 0050, Smooth On) into the moulds, the assembled chamber moulds are slid out once the silicone completely cures. In this way, the thread is partially embedded in the body of the robot. A thinner chamber mould is then inserted and cast into the inner side of the chamber, which fully integrates the thread into the silicone body. The next step is to seal the bottom and top of the robot using a harder silicone (DragonSkin 0030, Smooth On). Finally, the pneumatic pipes can be connected to the chambers via reserved holes. (c) Demoulding and finalising the robot: The last step is to attach connection plates to the fully demoulded robot.

which is proportional to the control signal ($0 \sim 10$ V), and an incorporated pressure feedback channel ($0 \sim 3$ bar). The pressure regulators are monitored and controlled by the NI-DAQ USB-6341, with multiple digital and analogue input/output ports. The input ports of all the pressure regulators are connected to a compressor (BAMBI MD Range Model 150/500). The NDI Aurora electromagnetic tracking system is used to monitor the configuration of the robots. The linear rail (Zaber X-LSM100A) with an attached 6 Degrees of Freedom (DoF) force/torque sensor (IIT-FT17) is designed to identify the stiffness of the robots. Matlab is used to collect and process the data with a 500 HZ acquisition frequency.

B. Experimental Protocols

Experiment 1 - Bending and Elongation: A 6 DoF NDI tracker was attached at the tip of each robot, from which the elongation ratio was calculated by variation of the position in the z-axis divided by the original length. The bending angle was calculated from the variation of the rotation matrix by Matlab function *quat2rotm()*. In the elongation test, all chambers were actuated simultaneously, with a maximum elongation ratio of 0.6. For the bending test, one chamber pair and two chamber pairs (for the type-1 robot) and one chamber and two chambers (for the the type-2 robot) actuation were both explored, with a maximum bending angle of $150°$.

Experiment 2 - Workspace: The pressure in each chamber of the robots was kept in the same range of $0 \sim 1.2$ bar, with an incremental step of 0.3 bar. In this way, there are a total of $5^3 = 125$ sets of pressurisation. The NDI tracker was attached at the tip of robots to record the position. The x-axis of the Aurora system aligns with the centre of a chamber (the type-2 robot) or a chamber pair (the type-1 robot).

Experiment 3 - Force Generation: The top of each robot was constrained by the force sensor, which prevents elongation and allows the blocked force to be measured. The robots were then actuated by one chamber (pair), two chamber(s) (pairs) and three chamber(s) (pairs) in turn, with the pressure in the range of $0 \sim 1.2$ bar for both manipulators. To prevent the robot from buckling when measuring the generated force under different pressure, a stiff rod was inserted into the inner lumen without influencing the measurement.

Experiment 4 - Stiffness: The stiffness was identified under four configurations: no pressurisation, one chamber actuated with a $90°$ bending angle, two chambers actuated with a $90°$ bending angle, and three chambers actuated with a 0.3 elongation ratio. The tip of the robot was pushed by the linear rail with the maximum deflection displacement Δ_d set as 15 mm and the speed as $0.25 \frac{\text{mm}}{\text{s}}$. The stiffness k can be calculated by $k = \frac{f_d}{\Delta_d}$, where f_d is the measured force. In each configuration, the stiffness along the x-, y- and z- axes were identified, and the stiffness is written in the tip frame.

C. Experimental Results

Results for Experiment 1: Fig. 4 shows the average elongation ratios (solid curves) and standard deviations (shaded areas) of four trials when one, two and three chambers are
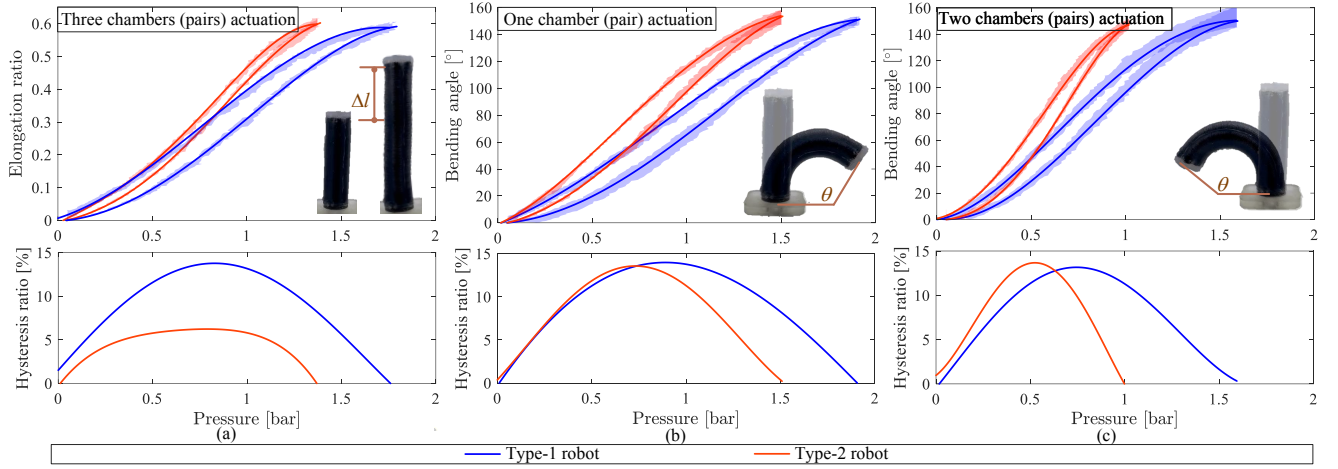
Fig. 4. Results for Experiment 1 - Elongation and bending response of each robot design under different actuation. (a) Elongation response with the corresponding hysteresis. (b) Bending angle response with the corresponding hysteresis when one of the three chambers is actuated. (c) Bending angle response with the corresponding hysteresis when two of the three chambers are actuated simultaneously.

actuated of the type-1 (blue colour) and type-2 (red colour) robot. The bottom row shows the calculated hysteresis based on average values. Fig. 4(a) illustrates the results when all chambers are actuated, requiring pressure to reach the elongation ratio of 0.60 is 1.80 bar for the type-1 robot and 1.40 bar for the type-2 robot, respectively. Based on the definition in Section II-C, β_e is 0.33/bar of the type-1 robot and 0.43/bar of the type-2 robot, indicating the actuation efficiency of elongation in the type-2 robot is 30.30% higher than that of the type-1 robot. The type-2 robot shows a lower hysteresis; the maximum hysteresis ratio of the type-1 robot

is 13.77%, whereas the value is 6.23% for the type-2 robot.

Figs. 4(b) and 4(c) show the bending results when one and two chambers are actuated. In particular, Fig. 4(b) shows the maximum pressure of the type-1 robot is 1.90 bar with the bending angle reaching 151.30°. In comparison, the pressure of the type-2 robot is 1.51 bar with a bending angle of 153.50°, from which the value of β_b of the type-1 and type-2 robot is 238.89°/bar and 304.97°/bar. Fig. 4(c) shows the results when two chamber pairs are actuated. Compared with Fig. 4(b), the required pressure to reach the same bending angle is smaller, i.e., 1.00 bar pressure can reach a bending angle of 148.12° for the type-2 robot; 1.60 bar pressure can reach 150.06° bending angle for the type-1 robot. When two chambers are actuated, the actuation ratio β_b of the type-1 and type-2 robot can then be calculated as 140.68°/bar and 222.18°/bar. By contrast, β_b of the type-1 robot with two actuated chambers decreases 41.11% compared to when one chamber is actuated, while β_b of the type-2 robot decreases 27.15%. The hysteresis ratios of all bending tests (see Figs. 4(b) and 4(c)) show a high consistency with values ranging from 13% ∼ 14%.

Results for Experiment 2: The results show the overall workspace of each robot has a domed shape, which is due to the elongation capability. The collected workspace points are projected onto the x-y, y-z and x-z plane to visualise and compare the differences, as explained further in Fig. 5.

Fig. 5 shows the workspace of each tested design is similar, but the overall workspace of the type-1 robot (blue colour) is smaller than the type-2 (red colour) robot under the same actuation pressure. The ranges of the reachable workspace of type-1 robot are [−39.01, 57.96] mm, [−40.15, 50.47] mm and [11.28, 73.46] mm along the x-, y- and z-axis, whereas the values for the type-2 robot are [−40.77, 68.51] mm, [−48.96, 57.00] mm and [−0.66, 77.79] mm, respectively. To quantitatively compare the two workspaces, the volume of the workspace is calculated using Matlab function *boundary()* with a shrink factor
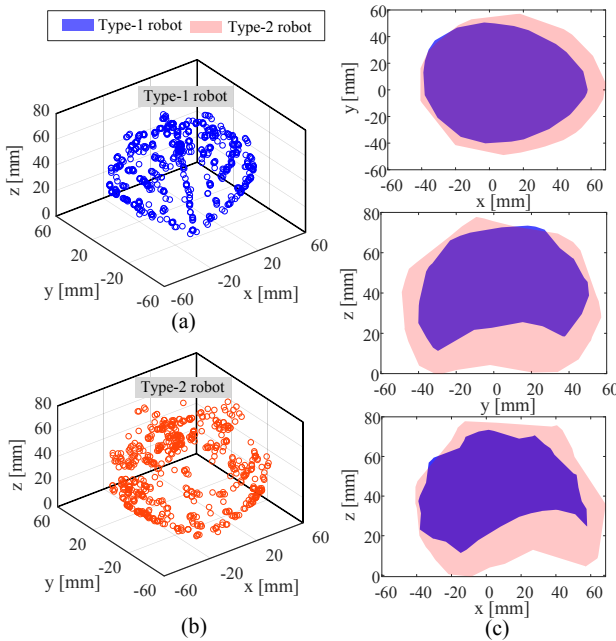

Fig. 5. Results for Experiment 2 - Workspace comparison of two robots under the same actuation. The reachable points of (a) the type-1 robot and (b) the type-2 robot in 3D space. (c) From the top to bottom: The projection of the workspace onto the x-y plane, y-z plane, x-z plane, respectively.
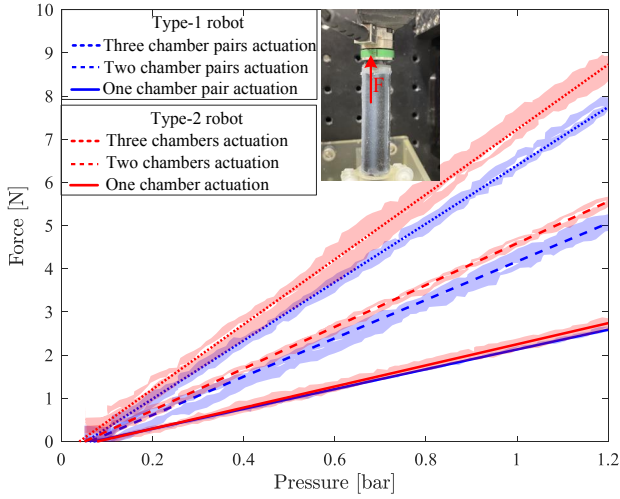
Fig. 6. Results of Experiment 3 - The comparison of the generated force under different actuation. Linear curve fitting is adopted.

of 1. The results show the volume is $43,327$ mm^3 and $59,213$ mm^3 for the type-1 and type-2 robot, which indicates the overall workspace of the type-2 robot is 36.67% larger than the type-1 robot with a maximum pressure of 1.2 bar.

Results for Experiment 3: In Fig. 6, the solid and dashed curves indicate which chambers are actuated, showing the average values and standard deviation of four trials of the blocked force measurements. The generated force is linearly proportional to the pressure for both robots, but the type-2 robot has better force generation capability than the type-1 robot. Specifically, Fig. 6 shows the maximum generated forces of the type-1 robot are 2.59 N, 5.10 N and 7.75 N when one, two and three chambers are actuated. The corresponding force-to-actuation ratio β_f can be calculated as 6.48 N/bar, 6.38 N/bar and 6.46 N/bar, showing high consistency. By contrast, the generated force of the type-2 robot is 2.75 N, 5.56 N and 8.75 N. Here, β_f is 6.87 N/bar, 6.95 N/bar and 7.29 N/bar, demonstrating a slight increase with greater pressurisation and leading to an overall higher β_f compared to the type-1 robot.

Results for Experiment 4: Fig. 7 illustrates the results of stiffness identification under four configurations (no actuation, one-, two- and three-chamber actuation). Again, the solid coloured curves show the average measurements and the shaded areas the standard deviations of four trials for the type-1 (blue colour) and type-2 (red colour) robot in x-, y- and z-direction. The first finding is that the overall stiffness decreases under higher pressurisation when the configuration is the same. Fig. 7(a) shows the initial stiffness along the x- and y- axis is $1.47 \times 10^{-2} \frac{\mathrm{N}}{\mathrm{mm}}$ for the type-1 robot, and $1.13 \times 10^{-2} \frac{\mathrm{N}}{\mathrm{mm}}$ for the type-2 robot; the stiffness along the z-axis is $1.19 \frac{\mathrm{N}}{\mathrm{mm}}$ for the type-1 robot and $0.91 \frac{\mathrm{N}}{\mathrm{mm}}$ for the type-2 robot. Fig. 7(d) shows the stiffness response under a 0.3 elongation ratio, which shows less stiffness compared with Fig. 7(a), i.e., the stiffness decreases to $0.60 \times 10^{-2} \frac{\mathrm{N}}{\mathrm{mm}}$ for the type-1 robot and $0.40 \times 10^{-2} \frac{\mathrm{N}}{\mathrm{mm}}$ for the type-2 robot. Comparing Fig. 7(b) with Fig. 7(c), the results demonstrate

a similar trend when the bending angle is the same.

The second finding is the overall stiffness of the type-1 robot is greater than that of the type-2 robot, evident from Figs. 7(a)-(d). Also, the buckling force of the type-1 robot is larger: The force is 5.57 N for the type-1 robot and 4.57 N for the type-2 robot, as shown in Fig. 7(a).

Thirdly, the stiffness of the two robots under investigation is configuration dependent. For example, comparing Fig. 7(a) with (b), the stiffness along the x-axis increases from $1.47 \times 10^{-2} \frac{\mathrm{N}}{\mathrm{mm}}$ to $1.53 \times 10^{-2} \frac{\mathrm{N}}{\mathrm{mm}}$ for the type-1 robot and from $1.13 \times 10^{-2} \frac{\mathrm{N}}{\mathrm{mm}}$ to $1.67 \times 10^{-2} \frac{\mathrm{N}}{\mathrm{mm}}$ for the type-1 robot.

D. Discussion

Both robots perform differently throughout Experiments 1-4, with the main comparisons summarised in Table I. These results indicate that chamber geometry plays a non-negligible role even when the initial chamber area is equivalent.

The type-2 robot shows better actuation efficiency than the type-1 robot, which essentially means less pressure is required to actuate the robot or generate force. However, the type-2 robot has comparatively lower stiffness than the type-1 robot, ranging from -18.97% to -26.93%. There are two reasons for this difference. Firstly, the distributed six circular chambers of the type-1 robot may provide a structural support for the robot. Secondly, the reinforced fibre constrains the perimeter of the chambers, and the chamber of the type-2 robot tends to converge to a circle from its initial semi-circular shape under the perimeter constraint [25]. This tendency means the equivalent chamber area of the type-2 robot increases under higher pressurisation. Evidence for this change is the force-actuation ratio of the type-1 robot remains $6.38 - 6.48$ N/bar in Experiment 3, whereas the ratio of the type-2 robot increases from 6.87 to 7.29 N/bar when the pressurisation varies from one chamber to three chambers.

Experiment 4 also shows the overall stiffness of each robot decreases with the increase of pressure, even if the pressurised chambers have a stiffening function [21]. An explanation for this behaviour is that silicone is incompressible and the longitudinal elongation reduces the radial diameter of the robot. In turn, the decrease of stiffness resulting from the elongation exceeds the increase of stiffness caused by the chamber stiffening. This is in line with the analysis by [31].

Experiment 1 shows even the elongation hysteresis of the type-2 robot is smaller than that of the type-1 robot, the bending hysteresis of both robots are on the same level. This may imply that the hysteresis mainly comes from the properties of elastomers, and the chamber geometries have small influence on the hysteresis.

With regards to the manufacturing process, the chamber design of the type-2 robot simplifies the fabrication process. Fewer chamber moulds are needed to construct the robot, and the fibre winding is halved. The overall improved actuation efficiency of the type-2 robot also provides the potential to further miniaturise the robot by reducing the size of actuation chambers, whereas scaling down the chamber size of the type-1 robot will compromise the actuation efficiency and increase the fabrication difficulties.
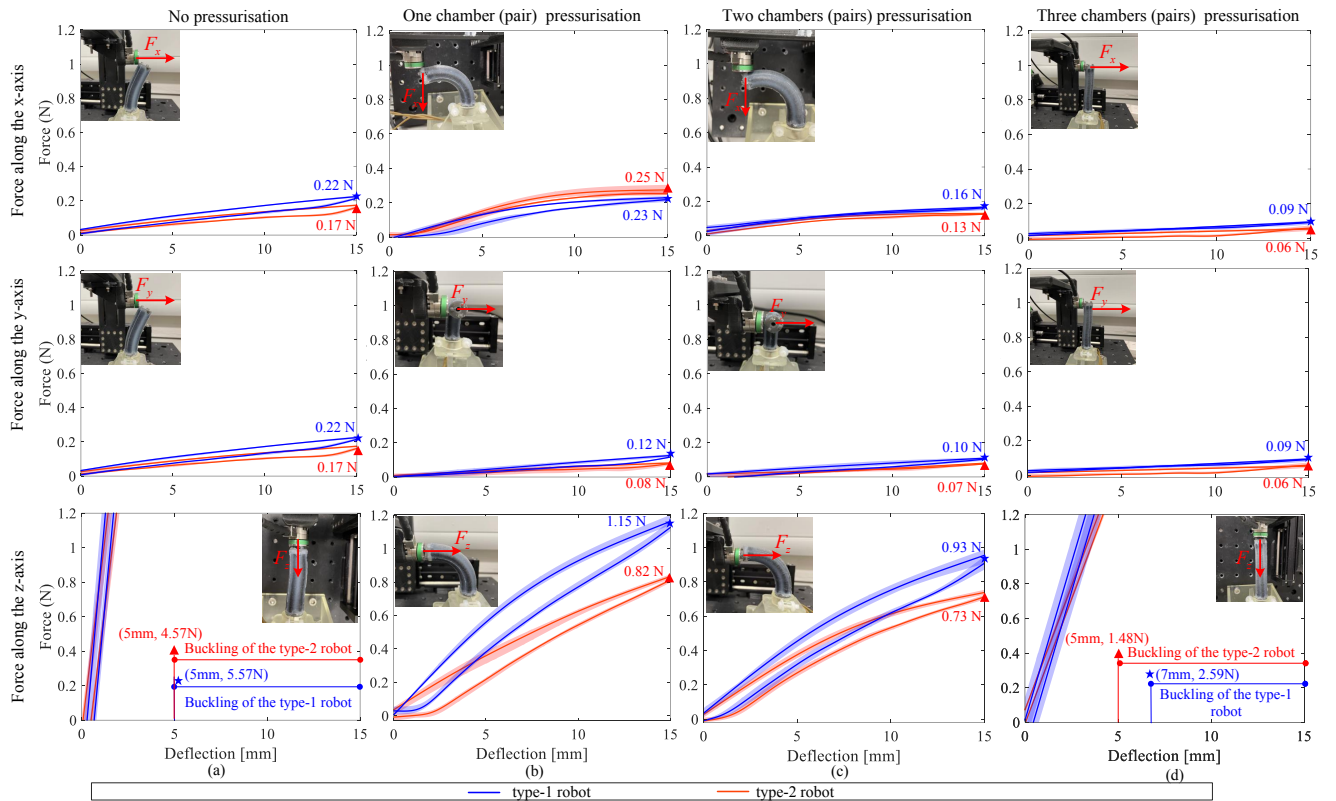
129

Fig. 7. Results of Experiment 4 - The stiffness identification written in the body frame. (a) The three directional stiffness when the robots are not pressurised. (b) The stiffness response when robots have a $90°$ bending angle when one chamber is pressurised. (c) The stiffness response when robots have a $90°$ bending angle with two chambers pressurised. (d) The stiffness response when robots have a 0.3 elongation ratio with three chambers pressurised.

IV. CONCLUSIONS

This research demonstrates how the design and fabrication of soft robots with different fibre-reinforced chambers can be streamlined, and investigates the impact of chamber geometry on the robots' performance. The experimental results indicate a semi-circular chamber design can improve actuation efficiency up to 57.93% and influence the stiffness of the robot up to 26.93%.

One future direction is to utilise the improved actuation efficiency of semi-circular chambers to further miniaturise the robotic manipulator to about 10 mm in diameter similar to standard rigid laparoscopic tools. This can facilitate the applications with limited allowable working spaces, such as MIS. Exploring robots, made of silicone with higher shore hardness values, will improve the robot's stiffness capability.

REFERENCES

[1] D. Rus and M. T. Tolley, "Design, fabrication and control of soft robots," *Nature*, vol. 521, no. 7553, pp. 467–475, 2015.

[2] A. Stilli, L. Grattarola, H. Feldmann, H. A. Wurdemann, and K. Althoefer, "Variable stiffness link (VSL): Toward inherently safe robotic manipulators," in *IEEE International Conference on Robotics and Automation*, 2017, pp. 4971–4976.

[3] A. B. Dawood, J. Fras, F. Aljaber, Y. Mintz, A. Arezzo, H. Godaba, and K. Althoefer, "Fusing dexterity and perception for soft robot-assisted minimally invasive surgery: What we learnt from STIFF-FLOP," *Applied Sciences*, vol. 11, no. 14, p. 6586, 2021.

[4] J. Fras, Y. Noh, M. Macias, H. Wurdemann, and K. Althoefer, "Bio-inspired octopus robot based on novel soft fluidic actuator," in *IEEE International Conference on Robotics and Automation*, 2018, pp. 1583–1588.

[5] L. Marechal, P. Balland, L. Lindenroth, F. Petrou, C. Kontovounisios, and F. Bello, "Toward a common framework and database of materials for soft robotics," *Soft Robotics*, vol. 8, no. 3, pp. 284–297, 2021.

[6] A. Shiva, S. H. Sadati, Y. Noh, J. Fraś, A. Ataka, H. Würdemann, H. Hauser, I. D. Walker, T. Nanayakkara, and K. Althoefer, "Elasticity versus hyperelasticity considerations in quasistatic modeling of a soft finger-like robotic appendage for real-time position and force estimation," *Soft Robotics*, vol. 6, no. 2, pp. 228–249, 2019.

[7] P. Polygerinos, N. Correll, S. A. Morin, B. Mosadegh, C. D. Onal, K. Petersen, M. Cianchetti, M. T. Tolley, and R. F. Shepherd, "Soft robotics: Review of fluid-driven intrinsically soft devices; manufacturing, sensing, control, and applications in human-robot interaction," *Advanced Engineering Materials*, no. 12, p. 1700016, 2017.

[8] A. D. Marchese, R. K. Katzschmann, and D. Rus, "A recipe for soft fluidic elastomer robots," *Soft robotics*, vol. 2, no. 1, pp. 7–25, 2015.

[9] Y. Elsayed, C. Lekakou, T. Geng, and C. M. Saaj, "Design optimisation of soft silicone pneumatic actuators using finite element analysis," in *IEEE/ASME International Conference on Advanced Intelligent Mechatronics*, 2014, pp. 44–49.

[10] L. Manfredi, E. Capoccia, G. Ciuti, and A. Cuschieri, "A soft pneumatic inchworm double balloon (SPID) for colonoscopy," *Scientific reports*, vol. 9, no. 1, pp. 1–9, 2019.

[11] K. Suzumori, S. Iikura, and H. Tanaka, "Applying a flexible microactuator to robotic mechanisms," *IEEE Control systems magazine*, vol. 12, no. 1, pp. 21–27, 1992.

[12] Z. Gong, X. Fang, X. Chen, J. Cheng, Z. Xie, J. Liu, B. Chen, H. Yang, S. Kong, Y. Hao, *et al.*, "A soft manipulator for efficient delicate grasping in shallow water: Modeling, control, and real-world experiments," *The International Journal of Robotics Research*, vol. 40, no. 1, pp. 449–469, 2021.

TABLE I
Summary of the Main Results from Experiments 1-4

	Exp. 1 - Actuation ratio			Exp. 2 - workspace	Exp. 3 - Force			Exp. 4 - Stiffness			
	Fig. 4(a) 3P β_e [/bar]	Fig. 4(b) 1P β_b [°/bar]	Fig. 4(c) 2P β_b [°/bar]	Fig. 5 Workspace volume [mm³]	3P [N/bar]	1P [N/bar]	2P [N/bar]	Fig. 7(a) 0P [N/mm]	Fig. 7(b) 1P [N/mm]	Fig. 7(c) 2P [N/mm]	Fig. 7(d) 3P [N/mm]
Type-1	0.33	238.89°	140.68°	43327	6.38	6.46	6.48	$\frac{(1.47,1.47,119)}{100}$	$\frac{(1.53,0.80,7.67)}{100}$	$\frac{(1.07,0.67,6.20)}{100}$	$\frac{(0.60,0.60,36.53)}{100}$
Type-2	0.43	304.97°	222.18°	59213	7.29	6.87	6.95	$\frac{(1.13,1.13,91)}{100}$	$\frac{(1.67,0.53,5.47)}{100}$	$\frac{(0.87,0.47,4.87)}{100}$	$\frac{(0.40,0.40,29.60)}{100}$
Diff.	30.30%	27.66%	57.93%	36.67%	14.26%	6.35%	7.25%	-23.53%	-26.93%	-21.49%	-18.97%

* 0P denotes no pressurisation; 1P denotes the pressurisation of one chamber; 2P denotes two chambers; 3P denotes three chambers. Stiffness here is a 3×1 vector with the form of (k_x, k_y, k_z), where k_x is the stiffness along the x- axis; k_y is the stiffness along the y- axis, k_z is the stiffness along the z- axis. The stiffness is compared using 2-norm.

[13] A. Shiva, A. Stilli, Y. Noh, A. Faragasso, I. De Falco, G. Gerboni, M. Cianchetti, A. Menciassi, K. Althoefer, and H. A. Wurdemann, "Tendon-based stiffening for a pneumatically actuated soft manipulator," *IEEE Robotics and Automation Letters*, vol. 1, no. 2, pp. 632–637, 2016.

[14] A. Jiang, E. Secco, H. Wurdemann, T. Nanayakkara, P. Dasgupta, and K. Athoefer, "Stiffness-controllable octopus-like robot arm for minimally invasive surgery," in *Workshop on New Technologies for Computer/Robot Assisted Surgery*, 2013, pp. 1–2.

[15] A. Palombi, G. M. Bosi, S. D. Giuseppe, E. De Momi, S. Homer-Vanniasinkam, G. Burriesci, and H. A. Wurdemann, "Sizing the aortic annulus with a robotised, commercially available soft balloon catheter: in vitro study on idealised phantoms," in *International Conference on Robotics and Automation*, 2019, pp. 6230–6236.

[16] H. A. Wurdemann, A. Stilli, and K. Althoefer, "Lecture notes in computer science: An antagonistic actuation technique for simultaneous stiffness and position control," in *Intelligent Robotics and Applications*, H. Liu, N. Kubota, X. Zhu, and R. Dillmann, Eds. Springer International Publishing, 2015, pp. 164–174.

[17] A. Stilli, K. Althoefer, and H. A. Wurdemann, *Soft Robotics. Bio-inspired Antagonistic Stiffening*. Springer International Publishing, 2018, pp. 207–214.

[18] G. Shi, A. Palombi, Z. Lim, A. Astolfi, A. Burani, S. Campagnini, F. G. C. Loizzo, M. L. Preti, A. M. Vargas, E. Peperoni, C. M. Oddo, M. Li, J. Hardwicke, M. Venus, S. Homer-Vanniasinkam, and H. A. Wurdemann, "Fluidic haptic interface for mechano-tactile feedback," *IEEE Transactions on Haptics*, vol. 13, no. 1, pp. 204–210, 2020.

[19] J. Fras, Y. Noh, H. Wurdemann, and K. Althoefer, "Soft fluidic rotary actuator with improved actuation properties," in *IEEE/RSJ International Conference on Intelligent Robots and Systems*, 2017, pp. 5610–5615.

[20] F. Connolly, P. Polygerinos, C. J. Walsh, and K. Bertoldi, "Mechanical programming of soft actuators by varying fiber angle," *Soft Robotics*, vol. 2, no. 1, pp. 26–32, 2015.

[21] H. Al-Fahaam, S. Nefti-Meziani, T. Theodoridis, and S. Davis, "The design and mathematical model of a novel variable stiffness extensor-contractor pneumatic artificial muscle," *Soft robotics*, vol. 5, no. 5, pp. 576–591, 2018.

[22] J. Fraś, J. Czarnowski, M. Maciaś, J. Główka, M. Cianchetti, and A. Menciassi, "New STIFF-FLOP module construction idea for improved actuation and sensing," in *IEEE International Conference on Robotics and Automation*, 2015, pp. 2901–2906.

[23] T. Ranzani, M. Cianchetti, G. Gerboni, I. De Falco, and A. Menciassi, "A soft modular manipulator for minimally invasive surgery: design and characterization of a single module," *IEEE Transactions on Robotics*, vol. 32, no. 1, pp. 187–200, 2016.

[24] H. Abidi, G. Gerboni, M. Brancadoro, J. Fras, A. Diodato, M. Cianchetti, H. Wurdemann, K. Althoefer, and A. Menciassi, "Highly dexterous 2-module soft robot for intra-organ navigation in minimally invasive surgery," *The International Journal of Medical Robotics and Computer Assisted Surgery*, vol. 14, no. 1, p. e1875, 2018.

[25] J. Fras and K. Althoefer, "Soft fiber-reinforced pneumatic actuator design and fabrication: Towards robust, soft robotic systems," in *Annual Conference Towards Autonomous Robotic Systems*, 2019, pp. 103–114.

[26] Y. Sun, S. Song, X. Liang, and H. Ren, "A miniature soft robotic manipulator based on novel fabrication methods," *IEEE Robotics and Automation Letters*, vol. 1, no. 2, pp. 617–623, 2016.

[27] G. Gerboni, T. Ranzani, A. Diodato, G. Ciuti, M. Cianchetti, and A. Menciassi, "Modular soft mechatronic manipulator for minimally invasive surgery (MIS): overall architecture and development of a fully integrated soft module," *Meccanica*, vol. 50, no. 11, pp. 2865–2878, 2015.

[28] J. Zhang, L. Liu, Y. Chen, M. Zhu, L. Tang, C. Tang, J. Shintake, J. Zhao, J. He, X. Ren, *et al.*, "Fiber-reinforced soft polymeric manipulator with smart motion scaling and stiffness tunability," *Cell Reports Physical Science*, p. 100600, 2021.

[29] M. Cianchetti, T. Ranzani, G. Gerboni, T. Nanayakkara, K. Althoefer, P. Dasgupta, and A. Menciassi, "Soft robotics technologies to address shortcomings in today's minimally invasive surgery: the STIFF-FLOP approach," *Soft robotics*, vol. 1, no. 2, pp. 122–131, 2014.

[30] S.-A. Abad, A. Arezzo, S. Homer-Vanniasinkam, and H. A. Wurdemann, "Soft robotic systems for endoscopic interventions," in *Endorobotics*, L. Manfredi, Ed. Academic Press, 2022, pp. 61–93.

[31] J. Shi, J. C. Frantz, A. Shariati, A. Shiva, J. S. Dai, D. Martins, and H. A. Wurdemann, "Screw theory-based stiffness analysis for a fluidic-driven soft robotic manipulator," in *IEEE International Conference on Robotics and Automation*, 2021, pp. 11 938–11 944.